AIP | Review of Scientific Instruments

X-ray imaging for studying behavior of liquids at high pressures and high temperatures using Paris-Edinburgh press

Yoshio Kono, Curtis Kenney-Benson, Yuki Shibazaki, Changyong Park, Yanbin Wang, and Guoyin Shen

Citation: Review of Scientific Instruments **86**, 072207 (2015); doi: 10.1063/1.4927227
View online: http://dx.doi.org/10.1063/1.4927227
View Table of Contents: http://scitation.aip.org/content/aip/journal/rsi/86/7?ver=pdfcov
Published by the AIP Publishing

X-ray imaging for studying behavior of liquids at high pressures and high temperatures using Paris-Edinburgh press

Yoshio Kono,[1] Curtis Kenney-Benson,[1] Yuki Shibazaki,[2] Changyong Park,[1] Yanbin Wang,[3] and Guoyin Shen[1]
[1]*HPCAT, Geophysical Laboratory, Carnegie Institution of Washington, 9700 S. Cass Ave., Argonne, Illinois 60439, USA*
[2]*Frontier Research Institute for Interdisciplinary Sciences, Tohoku University, Aramaki aza Aoba 6-3, Aoba-ku, Sendai 980-8578, Japan*
[3]*GeoSoilEnviroCARS, Center for Advanced Radiation Sources, The University of Chicago, 5640 S. Ellis Avenue, Chicago, Illinois 60637, USA*

(Received 9 February 2015; accepted 29 April 2015; published online 23 July 2015)

Several X-ray techniques for studying structure, elastic properties, viscosity, and immiscibility of liquids at high pressures have been integrated using a Paris-Edinburgh press at the 16-BM-B beamline of the Advanced Photon Source. Here, we report the development of X-ray imaging techniques suitable for studying behavior of liquids at high pressures and high temperatures. White X-ray radiography allows for imaging phase separation and immiscibility of melts at high pressures, identified not only by density contrast but also by phase contrast imaging in particular for low density contrast liquids such as silicate and carbonate melts. In addition, ultrafast X-ray imaging, at frame rates up to ~10^5 frames/second (fps) in air and up to ~10^4 fps in Paris-Edinburgh press, enables us to investigate dynamics of liquids at high pressures. Very low viscosities of melts similar to that of water can be reliably measured. These high-pressure X-ray imaging techniques provide useful tools for understanding behavior of liquids or melts at high pressures and high temperatures. © *2015 AIP Publishing LLC.* [http://dx.doi.org/10.1063/1.4927227]

I. INTRODUCTION

Knowledge of the structure, physical properties, and immiscibility behavior of melts at high pressures and high temperatures is important in industry as well as in understanding dynamics and evolution of the interiors of the Earth and other planets. Efforts have been made to investigate the structure (e.g., Refs. 1–4), physical properties such as density (e.g., Refs. 5–7), viscosity (e.g., Refs. 8–11), and elastic wave velocity (e.g., Refs. 12–14) of liquids. However, such experimental studies remain technologically challenging. Recently, an integrated setup for liquid structure, elastic wave velocity, and viscosity measurements has been developed using a Paris-Edinburgh (PE) cell at the 16-BM-B station, operated by the High Pressure Collaborative Access Team (HPCAT), at the Advanced Photon Source (APS), to investigate not only individual structure or properties of liquids but also the correlations between microscopic structure and macroscopic physical properties (cf. a review in Ref. 15).

X-ray imaging is one of the most powerful tools for investigating the behavior and properties of liquids. Falling sphere viscosity measurement is one of the most well established high-pressure X-ray imaging techniques used to investigate viscosity of liquids at high pressures (e.g., Refs. 8–11). In addition, high-pressure X-ray imaging studies have been conducted for studying surface tension on a liquid-liquid interface (e.g., Refs. 16 and 17) or immiscibility of liquids such as silicate melts and water (e.g., Refs. 18 and 19). Here, we describe the recent high-pressure X-ray imaging techniques developed at the 16-BM-B beamline. We first introduce our overall setup for studying structure and properties of liquids at high pressures (Section II), and then describe details of the X-ray imaging setup using white X-ray beam (Section III), followed by some experimental results of phase separation and liquid immiscibility (Section IV A) and falling sphere viscosity measurement for an ultralow viscous liquid (Section IV B).

II. PARIS-EDINBURGH CELL SETUP AT THE BEAMLINE 16-BM-B

Figure 1 shows the setup of the PE cell at 16-BM-B. The PE cell allows the usage of large sample volumes (up to 2 mm in both diameter and height) to pressures up to 7 GPa. A graphite heater in the cell assembly generates stable temperatures to 2000 °C, allowing us to study not only low melting temperature liquids such as sulfur[20] and cerium[21] but also high melting temperature liquids such as silicate melts (e.g., Refs. 4 and 22–24).

Structures of liquids are determined by a multi-angle energy dispersive X-ray diffraction technique combined with the PE cell (Refs. 4 and 15). A large Huber stage holding a Ge solid state detector allows precise control of 2θ angles from 2° to 39° (Fig. 1). Energy dispersive X-ray diffraction measurement using fine collimating slits provides good control of collimation depth, which is important for discriminating the weak liquid sample signal from background scattering caused by the surrounding capsule and/or pressure media (cf. Ref. 15). The wide horizontal opening of the PE cell is beneficial for the collection of energy dispersive X-ray diffraction patterns to high 2θ angles, allowing determination of structure factors of

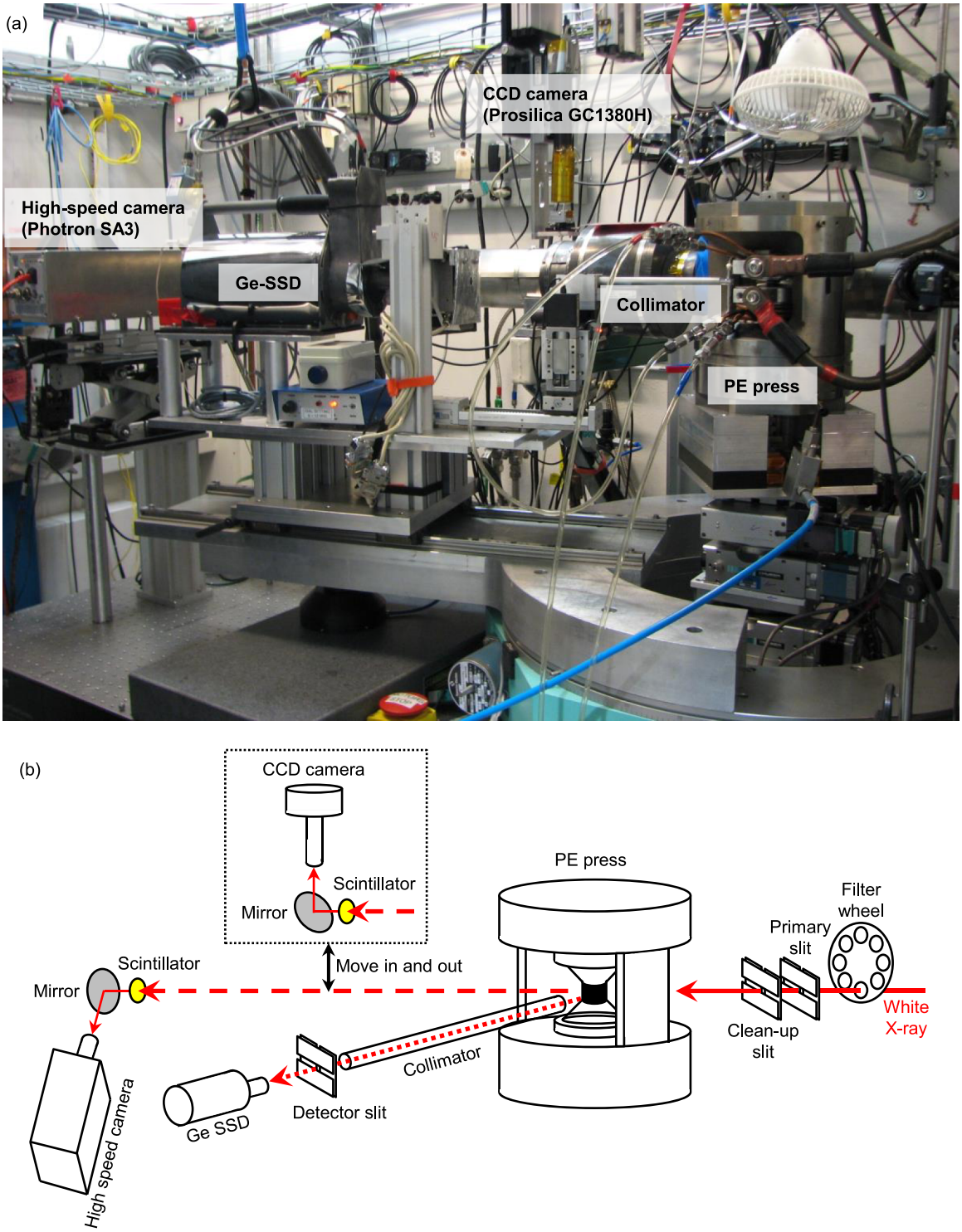

FIG. 1. A photograph (a) and schematic drawing (b) of the Paris-Edinburgh press experimental setup at the 16-BM-B beamline, HPCAT, at the Advanced Photon Source. Two cameras (Prosilica GC1380H and Photron SA3) are installed for X-ray imaging experiments.

liquids at large momentum transfer ($Q = 4\pi E \times \sin\theta/12.398$, where E is X-ray energy and θ is diffraction angle). Successful measurements of structure factors to high Q up to 22 $Å^{-1}$ for albite ($NaAlSi_3O_8$) melt at 5.3 GPa and 1600 °C have been demonstrated using the setup.[4] This method requires diffraction patterns at multiple angles to reliably derive structure factor information. The necessary number of 2θ angles depends on the system to be measured. A typical set includes eight to twelve 2θ angles covering from 2° to 39°. An analysis software package (aEDXD) has been developed and is available at HPCAT for structural analysis.[15]

In addition to the liquid structure measurement capability, the setup is integrated with instruments for measuring elastic wave velocity and viscosity. Elastic wave velocities (both V_p and V_s) are measured by the ultrasonic technique, in conjunction with sample length measurement by white X-ray radiography, not only for solid materials[25–28] but also for molten samples.[14,15] Details of the setup and analysis of the

ultrasonic measurement were described in Ref. 25. Viscosity is measured by falling sphere viscometry. A high-speed camera (Photron SA3) is used to study a wide range of viscosities of molten materials from liquid alkali halides[11] and carbonate melts[29] to silicate melts[30] at high pressure and high temperature conditions. Details of the viscosity measurement method are described in Refs. 11 and 15 with additional information in Section IV B of this paper. These physical property measurements (elastic wave velocity and/or viscosity) can be combined with structure measurement to study the correlations between macroscopic properties and atomistic structure at high pressure and high temperature conditions (e.g., Refs. 11, 25, and 27).

III. X-RAY IMAGING SETUP AT THE BEAMLINE 16-BM-B

A. Camera setup

High-pressure X-ray imaging is conducted using unfocused white X-ray at the 16-BM-B beamline. The beamline utilizes two cameras for X-ray imaging experiments. High spatial-resolution X-ray imaging measurements are conducted using a CCD camera (Prosilica GC1380H) placed roughly 30 cm from the sample position (Figure 1). A thin scintillator (5 μm thick Eu-doped lutetium aluminum garnet (LAG)) is used with a 45° mirror and a 10 times infinity-corrected objective lens mounted on a 127 mm long tube. Use of a thin scintillator is important for high spatial resolution,[31] but it decreases in detective quantum efficiency. It is known that a LAG scintillator has higher absorption than commonly available yttrium aluminum garnet (YAG) and provides better detective quantum efficiency.[32] By using the Eu-doped LAG scintillator, we can typically obtain a reasonable image with a 0.5 s exposure time.

The pixel resolution of the imaging setup is 0.95 μm/pixel and the full field of view is 1.3 (horizontal) mm × 1.0 (vertical) mm. The spatial resolution of this camera setup has been investigated in terms of the line spread function at a tungsten carbine (WC) plate edge.[15] The line spread function shows a sharpness of ~4 pixel (corresponding to ~4 μm), defined by the full width at the half maximum (FWHM), which may be viewed as the intrinsic imaging resolution of this X-ray radiography system. In addition, the precision in detecting the imaging changes was investigated by using a linear stage with 1 μm step to move the WC plate, resulting in a high precision with the 1σ standard deviation of 0.1 μm (Ref. 15). The camera is mainly used for determining sample length for the elastic wave velocity measurement[25] and sample size measurement.[21]

Another camera, a high-speed camera Photron SA3, is located approximately 1.2 m downstream from the PE cell (Figure 1). This camera is capable of imaging with a frame rate up to 1.2×10^5 frames/second (fps). We use 100 μm thick Ce-doped YAG as a scintillator. The thick YAG scintillator provides sufficiently high brightness for high-speed imaging in the PE press (cf. Section III C). We point out that use of a thick LAG scintillator will further improve the detective quantum efficiency and, consequently, the high-speed imaging capability. The pixel resolution is typically 4.9 μm/pixel using 5 times infinity-corrected objective lenses or 2.5 μm/pixel using 10 times infinity-corrected objective lenses. The full field of view is larger than the maximum sample size available in the PE cell (up to 2 mm in both diameter and height) (Ref. 15). The camera is used for phase contrast imaging and ultrafast imaging, both of which are described in more detail below.

B. Phase contrast imaging

Phase contrast imaging techniques are advantageous for imaging low-Z materials and low absorption contrast materials (e.g., see reviews in Ref. 33). In the absorption based X-ray imaging, the intensity pattern shows the density contrast in materials. In phase-contrast imaging, it records variations in the shape of an X-ray wavefront on passing through the sample. Intensity variations due to sharp changes in attenuation and refractive index in the sample can be detected, particularly for weakly absorbing materials. Several methods (e.g., interferometric technique, refraction-based technique, propagation-based technique) have been employed for phase contrast imaging (e.g., a review in Ref. 33). In particular, Ref. 34 demonstrated a simple method for phase contrast imaging using white X-rays based on a propagation-based technique. In the case of a highly spatially coherent beam, Fresnel diffraction is observed at a distance away from the sample, and edge-enhanced contrast can be observed at a distance away from an object without optics. The contrast increases with increasing distance between sample and detector (Ref. 34). Since this method requires no sophisticated X-ray optics or setup, it is suitable for application in high-pressure research where sample shape and position dynamically change with changing pressure and/or temperature conditions.

Figure 2 shows an example of images of air bubbles in epoxy at various distances from 15 cm to 75 cm. At the closest distance of 15 cm, the image mostly represents absorption contrast and it is difficult to see the air bubbles because of low Z and low density contrast between air and epoxy. At far distances, air bubbles can be viewed via the enhanced edges. The image obtained at a distance of 75 cm clearly shows various air bubbles with sizes ranging between ~25 and ~200 μm.

C. Ultrafast imaging capability

Figure 3 shows brightness variations in a series of images obtained of a ~150 μm diameter Pt sphere in a BN cup (2.4 mm outer diameter and ~0.3 mm inner diameter) with varying exposure times (camera frame rate) with and without the PE cell. The data show that, without the PE cell, quality imaging can be measured at a frame rate of 4×10^4 fps, while image brightness becomes insufficient at a frame rate of 10^5 fps. However, it is still possible to identify the Pt sphere in the BN cup in the image obtained at 10^5 fps by adjusting brightness and contrast of the image. These data show that the ultrafast imaging setup is capable of up to ~10^5 fps with 10 μs exposure time. On the other hand, the brightness of the image becomes significantly lower viewed through the PE cell due to absorption of X-rays by the pressure media (14 mm diameter boron epoxy, surrounding a 6 mm diameter MgO cylinder). There is sufficient brightness at 10^4 fps, but the brightness at 4×10^4 fps becomes too low to identify the Pt

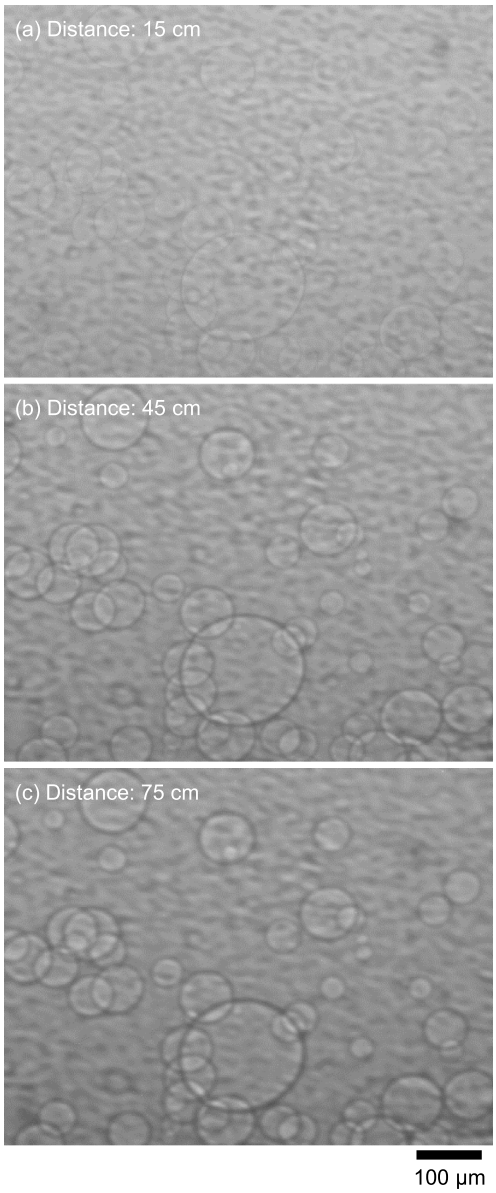

FIG. 2. X-ray images of air bubbles in epoxy obtained at camera distances of 15 cm (a), 45 cm (b), and 75 cm (c).

sphere. We therefore consider that the maximum frame rate available in the PE cell is around 10^4 fps. The maximum frame rate of 10^4 fps is much faster than those of previous high-speed imaging in large volume press (typically 30-60 fps and up to 125 fps) (Refs. 8–10, 35, and 36) and has allowed us to measure liquids with extremely low viscosities (Refs. 11 and 29).

IV. HIGH-PRESSURE X-RAY IMAGING EXPERIMENTS

A. Liquid phase separation and liquid-liquid immiscibility

Figure 4 shows the behavior of lithium germanate borate after melting at around 1.2 GPa in a BN capsule. The images are obtained by the Prosilica camera. The starting material is homogeneous lithium germanate borate glass synthesized by quenching from 1000 °C at ambient pressure. The sample melted at around 1000 °C and the shape changed slightly. The image of the sample immediately after melting has a homogeneous appearance without any visible texture. About 2 min after melting, the texture around the sample boundary started changing slightly, and then, 4 min after melting, the entire sample began to separate into 2 phases having low and high absorption. The darker portion condensed around the bottom of sample with time. Analysis of the quenched run product shows elemental germanium in a glassy matrix. These observations suggest that elemental germanium precipitated from homogeneous lithium germanate borate glass probably by reduction by BN capsule.

Imaging of phase separation may provide important knowledge on magmatic processes and chemical differentiation in the Earth's interior. For example, it is considered that the metallic core of the Earth is formed from extensively molten silicate layer (magma ocean) on the Earth's surface (e.g., Refs. 37 and 38). The first process of this model involves separation of liquid metal from silicate melt, with the metal droplets then falling into the magma ocean. High-pressure X-ray imaging may enable us to simulate these processes at high pressure and high temperature conditions of the Earth and planetary interiors and provides important knowledge on understanding the core formation process in the magma ocean model.

In addition, immiscibility of 2 liquid phases is important to understand the behavior of melt and the resultant geochemical and geophysical processes in the Earth's interior. It is known that several of Earth's melt compositions show immiscibility, such as silicate melt-H_2O system (e.g., Refs. 18 and 19), silicate and carbonate melt system (e.g., Refs. 39 and 40), iron-light element alloys (e.g., Refs. 41 and 42). *In situ* imaging of such behavior at high pressure and high temperature conditions would enhance our understanding of melt behavior in the Earth's interior. Some *in situ* X-ray imaging experiments have been conducted for silicate melt-H_2O system (e.g., Refs. 18 and 19) and iron-light element alloys (e.g., Ref. 42). However, it is difficult to monitor immiscibility of liquids having a small density difference such as silicate and carbonate melts.

Phase contrast imaging is a powerful tool to monitor low Z and low density contrast materials and is used to study immiscibility of silicate and carbonate melts with similar densities. We used the camera setup of the Photron SA3 (cf. Section III A) for the phase contrast imaging experiment. The long distance (~1.2 m) between the sample and the Photron SA3 camera setup was used to enhance the phase contrast for detecting immiscibility of silicate and carbonate melts. Figure 5 (Multimedia view) shows melting and subsequent behavior of silicate (albite: $NaAlSi_3O_8$) and carbonate ($CaCO_3$) melts. A previous quench experiment has reported immiscibility of albite and $CaCO_3$ melts at around 1350-1500 °C at 2.5 GPa for the compositions of around 50-70 wt. % of $CaCO_3$ in albite.[39] We conducted an *in situ* X-ray imaging experiment for a composition of ~60 wt. % of $CaCO_3$ in albite at ~2.5 GPa and ~1400 °C (Fig. 5) (Multimedia view). Albite and $CaCO_3$ were placed separately in the capsule. Melting began at the interface between albite and $CaCO_3$ and the entire sample was molten shortly. We succeeded in imaging the immiscibility of albite and $CaCO_3$ melts *in situ* at high pressure

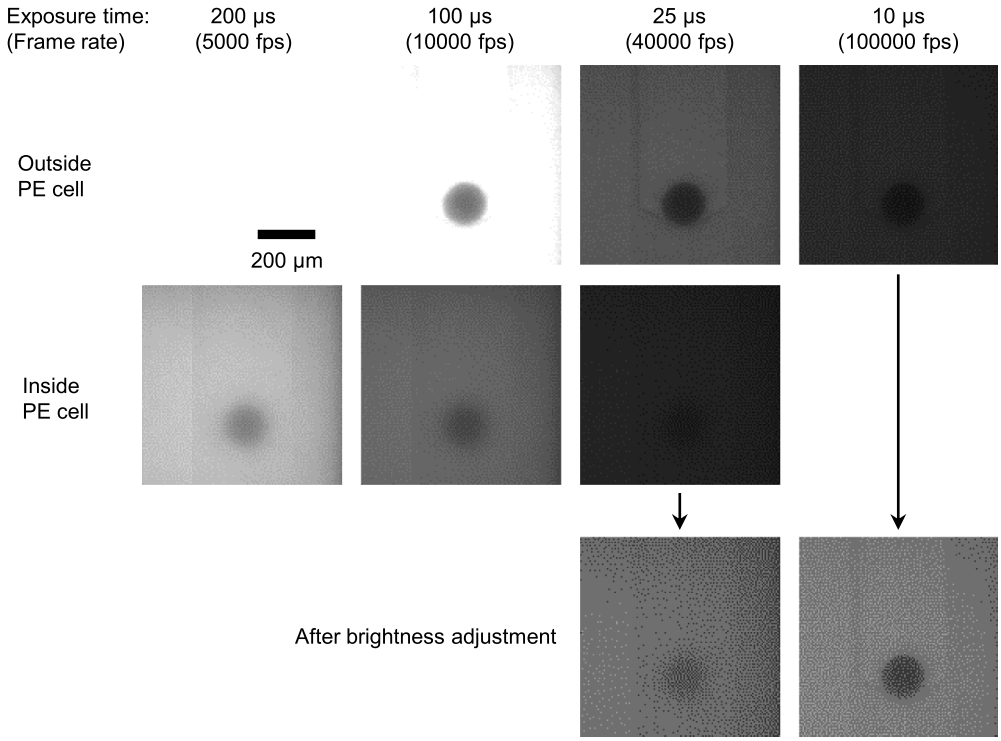

FIG. 3. X-ray images of a Pt sphere in a BN cup inside or outside a Paris-Edinburgh cell obtained by high speed camera. The X-ray images were obtained at various exposure times from 10 μs to 200 μs, corresponding to camera frame rates of 5×10^3-10^5 frames/s.

and high temperature conditions. These 2 liquids show very weak absorption contrast due to their very similar densities,[43] while the boundaries are clearly detected in phase contrast imaging.

B. Falling sphere viscosity measurement for ultralow viscous liquid

Falling sphere viscosity measurement is based on the Stokes' equation. The viscosity (η) can be calculated via the Stokes' equation with correction factors for the effect of both the wall (F) (Ref. 44) and the end (E) (Ref. 45) of a cylindrical sample container,

$$\eta = \frac{g d_s^2 (\rho_s - \rho_l)}{18\nu} \frac{F}{E}, \quad (1)$$

$$F = 1 - 2.104\left(\frac{d_s}{d_l}\right) + 2.09\left(\frac{d_s}{d_l}\right)^3 - 0.95\left(\frac{d_s}{d_l}\right)^5, \quad (2)$$

$$E = 1 + \frac{9}{8}\frac{d_s}{2Z} + \left(\frac{9}{8}\frac{d_s}{2Z}\right)^2, \quad (3)$$

where ρ and d are density and diameter, with subscripts s and l denoting properties of the probing sphere and liquid sample, respectively. Z is the sample height. ν is terminal velocity of the falling sphere. It has been pointed out that uncertainties in terminal velocity play a dominant role in the precision of the viscosity determination.[46] For liquid samples with identical sphere and container geometries, the precision of the terminal velocity measurement depends primarily on the camera frame rate.

Figure 6 shows falling velocity determined in previous studies (Refs. 8–10, 35, and 36) and in recent studies conducted at the beamline 16-BM-B (Refs. 11, 15, 29, and 47) as a function of camera frame rate. The lines represent the number of points which can be obtained in a 1 mm falling distance. The calculation implies that the previously used 30-60 fps

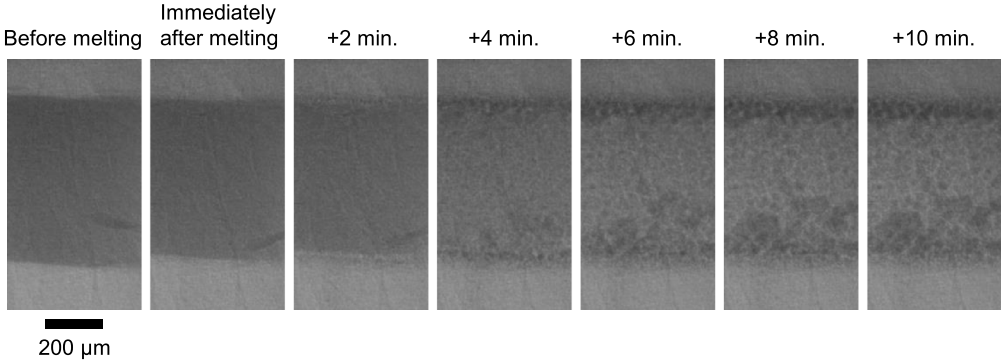

FIG. 4. Melting and the subsequent phase separation in lithium germanate borate melt at ~1.2 GPa and ~1000 °C.

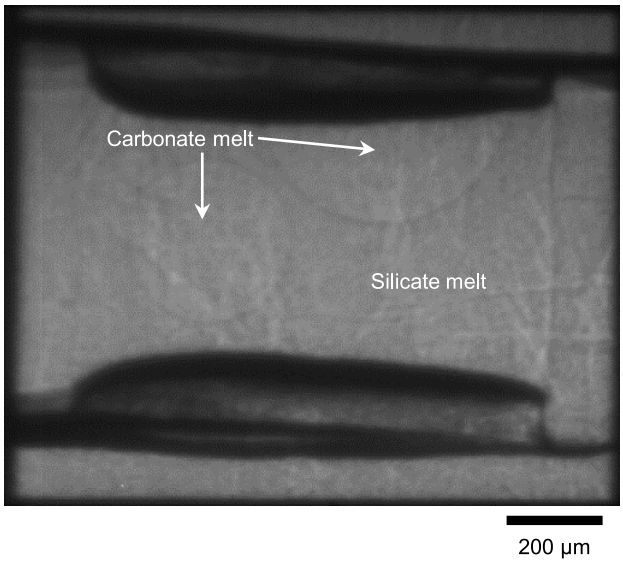

FIG. 5. X-ray imaging obtained for an albite ($NaAlSi_3O_8$) and $CaCO_3$ mixture at ~2.5 GPa and ~1400 °C. The sample was capsulated in a sapphire single crystal sleeve with a Pt foil cap. The X-ray image shows co-existence of two melt phases with boundaries enhanced by phase contrast rather than absorption contrast. The movie was recorded with the frame rate of 60 frames/s and it displays at 10 times faster speed. The actual length of the movie is 100 s. (Multimedia view) [URL: http://dx.doi.org/10.1063/1.4927227.1]

cameras can record only a few frames during the fall of the sphere in low viscous liquids. In fact, some studies determined viscosity based on only 2-4 images (e.g., Refs. 8–10). When such limited imaging rates are used, it is difficult to correctly discern when the falling sphere has reached terminal velocity, which, in turn, leads to large uncertainties in the calculated viscosity. In contrast, ultrafast imaging with $>10^3$ fps allows for monitoring the motion of the falling sphere with substantial oversampling, resulting in accurate determination of terminal velocity. Ultrafast imaging, up to 10^4 fps, is critical to our falling sphere viscosity measurements of ultralow viscosity liquids.

Supplementary Movie 1 (Ref. 48) shows the fastest falling sphere viscosity measurement conducted, to date, using the ultrafast imaging setup at the 16-BM-B beamline. Figure 7 shows a series of selected images of the WC sphere at various times during the fall (Fig. 7(a)), as well as the sphere travel distance and velocity as a function of elapsed time (Fig. 7(b)). This viscosity measurement was conducted for liquid sulfur at 3.8 GPa and 1430 °C. Supplementary Movie 1 (Ref. 48) was recorded at 5×10^3 fps (exposure time of 200 μs) and plays back at a reduced frame rate of 25 fps (200 times slower display). At the starting point of the Supplementary Movie 1 (Ref. 48), the temperature is higher than the melting point of the sulfur sample, which is molten. A WC sphere (200 μm diameter) is held by solid NaCl on the top of the liquid sulfur. When the temperature reached the melting temperature of NaCl, it melts and the WC sphere starts to fall. However, the WC sphere does not directly fall into liquid sulfur. The WC sphere temporarily stopped at the interface between liquid NaCl and liquid sulfur. The WC sphere stayed at the interface for around 60 ms and then fell into the liquid sulfur. We found a very fast falling speed for the WC sphere in liquid sulfur, with

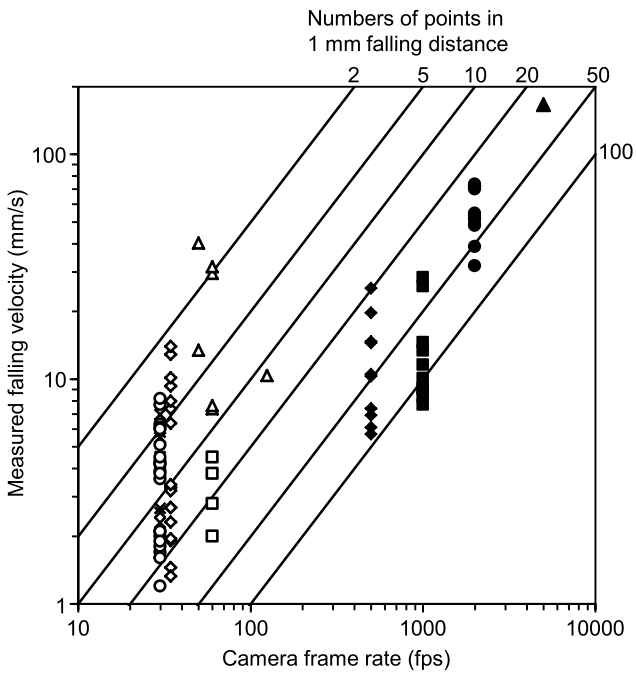

FIG. 6. Falling velocities measured in previous studies (cross: Ref. 8, open diamond: Ref. 9, open square: Ref. 10, open circle: Ref. 35, open triangle: Ref. 36) compared to those measured at 16-BM-B (solid circle: Ref. 11, solid square: Ref. 29, solid diamond: Ref. 47, solid triangle: this study) as a function of camera frame rate. Lines represent the estimated numbers of points that can be recorded in 1 mm falling distance.

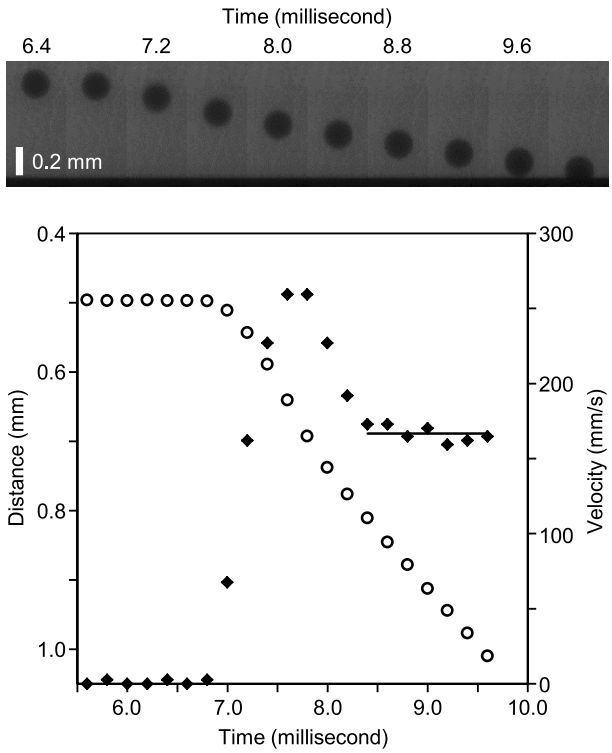

FIG. 7. X-ray radiography images of a falling WC sphere (200 μm) in liquid sulfur at 3.8 GPa and 1430 °C (a). (b) The results of the falling distance (open circles) and the falling velocity (solid diamonds) for each frame (200 μs interval). The data show high falling velocity as the WC sphere passes through the interface between liquid NaCl and liquid sulfur, which is interpreted as the influence of an interfacial tension force, after which the WC sphere falls in liquid sulfur at a terminal velocity of 167 mm/s.

the WC sphere falling ~0.5 mm in just 2.5 ms (Fig. 7(b)). We succeeded in monitoring the fall of the WC sphere through 13 frames using an ultrafast imaging rate of 5×10^3 fps.

The result shows a high falling velocity at the beginning of the drop, around the interface between liquid NaCl and liquid sulfur, and then a terminal velocity reached at 8.4-9.6 ms. The high falling velocity near the interface is interpreted by a model for the transport process that applies then the interfacial tension force is larger than the gravitational force.[49] According to the model, sphere falling velocity is reduced as the sphere approaches an interface which deforms. Then, the capillary waves of the interface connect to the wetting layer surrounding the sphere. This connection grows as the sphere is dragged through the interface, and consequently, the sphere is accelerated by the capillary forces. In fact, the deformation of the liquid-liquid interface and the motion of the interface while the sphere passes through it can be seen in our experiment (Supplementary Movie 2 (Ref. 48)). We therefore consider the influence of the interfacial tension force to be the cause of the high velocity measured at the beginning of the sphere's fall.

We obtain a constant terminal velocity of 167 ± 5 mm/s at 8.4-9.6 ms. Given the experimental parameters for Equations (1)-(3) (ρ_s = 14.74 g/cm^3 (Ref. 50), ρ_l = 1.1 g/cm^3 (Ref. 51), d_s = 0.2 mm, d_l = 1.5 mm, Z = 0.7 mm), we obtained a viscosity of 1.09 mPa s for liquid sulfur at 3.8 GPa and 1430 °C, which is very close to that of water (1.002 mPa s) at 1 atm and 20 °C (Ref. 52). The falling sphere viscometry using ultrafast imaging is an effective method to study viscosity of such ultralow viscous liquids at high pressure and high temperature conditions.

ACKNOWLEDGMENTS

We acknowledge an anonymous reviewer for valuable comments. This research is supported by DOE Nos. DE-FG02-99ER45775 and DE-NA0001974. This work was performed at HPCAT (Sector 16), Advanced Photon Source (APS), Argonne National Laboratory. HPCAT operations are supported by DOE-NNSA under Award No. DE-NA0001974 and DOE-BES under Award No. DE-FG02-99ER45775. The Advanced Photon Source is a U.S. Department of Energy (DOE) Office of Science User Facility operated for the DOE Office of Science by Argonne National Laboratory under Contract No. DE-AC02-06CH11357. The Paris-Edinburgh cell program is partly supported by GeoSoilEnviroCARS (GSECARS), which is supported by the National Science Foundation—Earth Sciences (No. EAR-1128799) and Department of Energy—GeoSciences (No. DE-FG02-94ER14466). Y.W. acknowledges NSF Grant No. EAR-1214376.

[1]K. Tsuji, K. Yaoita, M. Imai, O. Shimomura, and T. Kikegawa, Rev. Sci. Instrum. **60**(7), 2425–2428 (1989).
[2]M. Mezouar, P. Faure, W. Crichton, N. Rambert, B. Sitaud, S. Bauchau, and G. Blattmann, Rev. Sci. Instrum. **73**(10), 3570–3574 (2002).
[3]G. Shen, V. B. Prakapenka, M. L. Rivers, and S. R. Sutton, Phys. Rev. Lett. **92**(18), 185701 (2004).
[4]A. Yamada, Y. Wang, T. Inoue, W. Yang, C. Park, T. Yu, and G. Shen, Rev. Sci. Instrum. **82**(1), 015103 (2011).
[5]Y. Katayama, K. Tsuji, O. Shimomura, T. Kikegawa, M. Mezouar, D. Martinez-Garcia, J. M. Besson, D. Hausermann, and M. Hanfland, J. Synchrotron Radiat. **5**(3), 1023–1025 (1998).
[6]G. Shen, N. Sata, M. Newville, M. L. Rivers, and S. R. Sutton, Appl. Phys. Lett. **81**(8), 1411–1413 (2002).
[7]E. Ohtani, A. Suzuki, R. Ando, S. Urakawa, K. Funakoshi, and Y. Katayama, in *Advances in High-Pressure Technology for Geophysical Applications*, edited by J. Chen, Y. Wang, T. S. Duffy, G. Shen, and L. F. Dobrzhinetskaya (Elsevier, Amsterdam, 2005), pp. 195–210.
[8]D. P. Dobson, W. A. Crichton, L. Vocadlo, A. P. Jones, Y. Wang, T. Uchida, M. Rivers, S. Sutton, and J. P. Brodholt, Am. Mineral. **85**(11-12), 1838–1842 (2000).
[9]H. Terasaki, T. Kato, S. Urakawa, K.-i. Funakoshi, A. Suzuki, T. Okada, M. Maeda, J. Sato, T. Kubo, and S. Kasai, Earth Planet. Sci. Lett. **190**(1–2), 93–101 (2001).
[10]J.-P. Perrillat, M. Mezouar, G. Garbarino, and S. Bauchau, High Pressure Res. **30**(3), 415–423 (2010).
[11]Y. Kono, C. Kenney-Benson, C. Park, G. Shen, and Y. Wang, Phys. Rev. B **87**(2), 024302 (2013).
[12]F. Decremps, L. Belliard, B. Couzinet, S. Vincent, P. Munsch, G. Le Marchand, and B. Perrin, Rev. Sci. Instrum. **80**(7), 073902 (2009).
[13]K. Nishida, Y. Kono, H. Terasaki, S. Takahashi, M. Ishii, Y. Shimoyama, Y. Higo, K.-i. Funakoshi, T. Irifune, and E. Ohtani, Earth Planet. Sci. Lett. **362**, 182–186 (2013).
[14]Z. Jing, Y. Wang, Y. Kono, T. Yu, T. Sakamaki, C. Park, M. L. Rivers, S. R. Sutton, and G. Shen, Earth Planet. Sci. Lett. **396**, 78–87 (2014).
[15]Y. Kono, C. Park, C. Kenney-Benson, G. Shen, and Y. Wang, Phys. Earth Planet. Inter. **228**, 269–280 (2014).
[16]H. Terasaki, S. Urakawa, K. Funakoshi, N. Nishiyama, Y. Wang, K. Nishida, T. Sakamaki, A. Suzuki, and E. Ohtani, Phys. Earth Planet. Inter. **174**(1), 220–226 (2009).
[17]H. Terasaki, S. Urakawa, D. C. Rubie, K.-i. Funakoshi, T. Sakamaki, Y. Shibazaki, S. Ozawa, and E. Ohtani, Phys. Earth Planet. Inter. **202**, 1–6 (2012).
[18]K. Mibe, M. Kanzaki, T. Kawamoto, K. N. Matsukage, Y. Fei, and S. Ono, J. Geophys. Res.: Solid Earth **112**(B3), B03201, doi: 10.1029/2005jb004125 (2007).
[19]T. Kawamoto, M. Kanzaki, K. Mibe, K. N. Matsukage, and S. Ono, Proc. Natl. Acad. Sci. U. S. A. **109**(46), 18695–18700 (2012).
[20]L. Liu, Y. Kono, C. Kenney-Benson, W. Yang, Y. Bi, and G. Shen, Phys. Rev. B **89**(17), 174201 (2014).
[21]M. J. Lipp, Z. Jenei, D. Ruddle, C. Aracne-Ruddle, H. Cynn, W. J. Evans, Y. Kono, C. Kenney-Benson, and C. Park, J. Phys.: Conf. Ser. **500**, 032011 (2014).
[22]T. Sakamaki, Y. Wang, C. Park, T. Yu, and G. Shen, J. Appl. Phys. **111**(11), 112623 (2012).
[23]C. Sanloup, J. W. E. Drewitt, C. Crépisson, Y. Kono, C. Park, C. McCammon, L. Hennet, S. Brassamin, and A. Bytchkov, Geochim. Cosmochim. Acta **118**, 118–128 (2013).
[24]Y. Wang, T. Sakamaki, L. B. Skinner, Z. Jing, T. Yu, Y. Kono, C. Park, G. Shen, M. L. Rivers, and S. R. Sutton, Nat. Commun. **5**, 3241 (2014).
[25]Y. Kono, C. Park, T. Sakamaki, C. Kenny-Benson, G. Shen, and Y. Wang, Rev. Sci. Instrum. **83**(3), 033905 (2012).
[26]M. J. Lipp, Y. Kono, Z. Jenei, H. Cynn, C. Aracne-Ruddle, C. Park, C. Kenney-Benson, and W. J. Evans, J. Phys.: Condens. Matter **25**(34), 345401 (2013).
[27]T. Sakamaki, Y. Kono, Y. Wang, C. Park, T. Yu, Z. Jing, and G. Shen, Earth Planet. Sci. Lett. **391**, 288–295 (2014).
[28]Q. Zeng, Y. Kono, Y. Lin, Z. Zeng, J. Wang, S. V. Sinogeikin, C. Park, Y. Meng, W. Yang, and H.-K. Mao, Phys. Rev. Lett. **112**(18), 185502 (2014).
[29]Y. Kono, C. Kenney-Benson, D. Hummer, H. Ohfuji, C. Park, G. Shen, Y. Wang, A. Kavner, and C. E. Manning, Nat. Commun. **5**, 5091 (2014).
[30]H. Spice, C. Sanloup, B. Cochain, C. De Grouchy, and Y. Kono, Geochim. Cosmochim. Acta **148**, 219–227 (2015).
[31]A. Koch, C. Raven, P. Spanne, and A. Snigirev, J. Opt. Soc. Am. A **15**(7), 1940–1951 (1998).
[32]A. Koch, F. Peyrin, P. Heurtier, B. Ferrand, B. Chambaz, W. Ludwig, and M. Couchaud, SPIE **3659**, 170–179 (1999).
[33]A. Momose, Jpn. J. Appl. Phys. **44**(9R), 6355 (2005).
[34]S. W. Wilkins, T. E. Gureyev, D. Gao, A. Pogany, and A. W. Stevenson, Nature **384**(6607), 335–338 (1996).
[35]C. Liebske, B. Schmickler, H. Terasaki, B. T. Poe, A. Suzuki, K.-i. Funakoshi, R. Ando, and D. C. Rubie, Earth Planet. Sci. Lett. **240**(3), 589–604 (2005).
[36]H. Terasaki, A. Suzuki, E. Ohtani, K. Nishida, T. Sakamaki, and K. Funakoshi, Geophys. Res. Lett. **33**(22), L22307, doi: 10.1029/2006GL027147 (2006).

[37]D. C. Rubie, H. J. Melosh, J. E. Reid, C. Liebske, and K. Righter, Earth Planet. Sci. Lett. **205**(3), 239–255 (2003).
[38]B. J. Wood, M. J. Walter, and J. Wade, Nature **441**(7095), 825–833 (2006).
[39]W.-j. Lee and P. J. Wyllie, J. Petrol. **37**(5), 1125–1152 (1996).
[40]W. G. Minarik, J. Petrol. **39**(11-12), 1965–1973 (1998).
[41]C. Sanloup and Y. Fei, Phys. Earth Planet. Inter. **147**(1), 57–65 (2004).
[42]K. Tsuno, H. Terasaki, E. Ohtani, A. Suzuki, Y. Asahara, K. Nishida, T. Sakamaki, K. i. Funakoshi, and T. Kikegawa, Geophys. Res. Lett. **34**(17), L17303, doi: 10.1029/2007GL030750 (2007).
[43]M. J. Genge, G. D. Price, and A. P. Jones, Earth Planet. Sci. Lett. **131**(3–4), 225–238 (1995).
[44]H. Faxén, Ark. Mat., Astron. Fys. **19**, 1–8 (1925).
[45]A. D. Maude, Br. J. Appl. Phys. **12**(6), 293–295 (1961).
[46]M. Brizard, M. Megharfi, and C. Verdier, Metrologia **42**, 298–303 (2005).
[47]Y. Kono, C. Kenney-Benson, Y. Shibazaki, C. Park, G. Shen, and Y. Wang, Phys. Earth Planet. Inter. **241**, 57–64 (2015).
[48]See supplementary material at http://dx.doi.org/10.1063/1.4927227 for the movies for falling of a WC sphere in liquid sulfur. Supplementary Movie 1 was recorded with the frame rate of 5000 frames/s and it displays by 25 frames/s (200 times slower display). The actual length of the movie is 92 ms. Supplementary Movie 2 displays selected region from Supplementary Movie 1. The movie displays by 5 frames/s (1000 times slower display). Actual length of the movie is 6.6 ms.
[49]J. W. J. De Folter, V. W. A. De Villeneuve, D. G. A. L. Aarts, and H. N. W. Lekkerkerker, New J. Phys. **12**(2), 023013 (2010).
[50]K. D. Litasov, A. Shatskiy, Y. Fei, A. Suzuki, E. Ohtani, and K. Funakoshi, J. Appl. Phys. **108**(5), 053513 (2010).
[51]K.-i. Funakoshi and A. Nozawa, Rev. Sci. Instrum. **83**(10), 103908 (2012).
[52]L. Korson, W. Drost-Hansen, and F. J. Millero, J. Phys. Chem. **73**(1), 34–39 (1969).